

See discussions, stats, and author profiles for this publication at: <https://www.researchgate.net/publication/11766650>

# Schuler, W., Kloiber, K., Matt, T., Bister, K. & Konrat, R. Application of cross-correlated NMR spin relaxation to the zinc-finger protein CRP2(LIM2): evidence for collective moti...

ARTICLE *in* BIOCHEMISTRY · SEPTEMBER 2001

Impact Factor: 3.02 · DOI: 10.1021/bi010509m · Source: PubMed

---

CITATIONS

11

---

READS

19

5 AUTHORS, INCLUDING:



[Theresia Dunzendorfer-Matt](#)

Medizinische Universität Innsbruck

10 PUBLICATIONS 248 CITATIONS

SEE PROFILE



[Klaus Bister](#)

University of Innsbruck

117 PUBLICATIONS 3,385 CITATIONS

SEE PROFILE



[Robert Konrat](#)

University of Vienna

134 PUBLICATIONS 2,966 CITATIONS

SEE PROFILE

# Application of Cross-Correlated NMR Spin Relaxation to the Zinc-Finger Protein CRP2(LIM2): Evidence for Collective Motions in LIM Domains<sup>†,‡</sup>

Wolfgang Schüler,<sup>§</sup> Karin Kloiber,<sup>§</sup> Theresia Matt,<sup>||</sup> Klaus Bister,<sup>||</sup> and Robert Konrat<sup>\*,§</sup>

*Institute of Organic Chemistry and Institute of Biochemistry, University of Innsbruck, A-6020 Innsbruck, Austria*

*Received March 12, 2001; Revised Manuscript Received May 11, 2001*

**ABSTRACT:** The solution structure of quail CRP2(LIM2) was significantly improved by using an increased number of NOE constraints obtained from a <sup>13</sup>C,<sup>15</sup>N-labeled protein sample and by applying a recently developed triple-resonance cross-correlated relaxation experiment for the determination of the backbone dihedral angle  $\psi$ . Additionally, the relative orientation of the <sup>15</sup>N(*i*)–<sup>1</sup>H<sup>N</sup>(*i*) dipole and the <sup>13</sup>CO(*i*) CSA tensor, which is related to both backbone angles  $\varphi$  and  $\psi$ , was probed by nitrogen–carbonyl multiple-quantum relaxation and used as an additional constraint for the refinement of the local geometry of the metal-coordination sites in CRP2(LIM2). The backbone dynamics of residues located in the folded part of CRP2(LIM2) have been characterized by proton-detected <sup>13</sup>C′(*i*–1)–<sup>15</sup>N(*i*) and <sup>15</sup>N(*i*)–<sup>1</sup>H<sup>N</sup>(*i*) multiple-quantum relaxation, respectively. We show that regions having cross-correlated time modulation of backbone isotropic chemical shifts on the millisecond to microsecond time scale correlate with residues that are structurally altered in the mutant protein CRP2(LIM2)R122A (disruption of the CCHC zinc-finger stabilizing side-chain hydrogen bond) and that these residues are part of an extended hydrogen-bonding network connecting the two zinc-binding sites. This indicates the presence of long-range collective motions in the two zinc-binding subdomains. The conformational plasticity of the LIM domain may be of functional relevance for this important protein recognition motif.

The LIM<sup>1</sup> domain is composed of a cysteine-rich motif that was first observed in the protein products of three regulatory genes (*I*, *2*) and contains two closely spaced tetrahedral Zn(II)-coordinating sites of the CCHC and CCCC type, capable of binding two zinc ions (3–5). The LIM domain proteins constitute a superfamily of proteins with diverse biochemical functions. Members of the family are LIM-homeodomain (LIM-HD), LIM-only proteins, or proteins containing additional functional domains of various types (e.g., kinase domains) (6–9). Most family members are presumably involved in protein–protein interactions; for example, LIM-HD proteins interact with the transcriptional machinery (10).

The *CSRP* genes encode a specific class of LIM-only proteins, termed cysteine-rich proteins (CRP) comprising two LIM domains (11). The CRP proteins characterized to date are involved in the regulation of cell differentiation and proliferation, particularly muscle differentiation (12, 13). Biophysical studies have revealed that a single LIM domain

acts as a specific and distinct protein-binding interface (14–17).

Three-dimensional structures of several LIM domains have been determined (18–25). It was shown that all LIM domains share a unique globular fold and consist of CCHC and CCCC zinc-binding subdomains tightly packed via a hydrophobic core region with distinct aliphatic and aromatic side-chain interactions. Further insight into the structural characteristics of a LIM domain was obtained from NMR structural studies of point mutants of CRP2(LIM2), CRP2-(LIM2)E155G (22) and CRP2(LIM2)R122A (24). One of these studies provided further insight into the structural determinants of the LIM domain fold and demonstrated the importance of side-chain hydrogen bonds for the stabilization of the metal coordinating “rubredoxin (Rd) knuckles” (22). The disruption of this extended hydrogen-bonding network in the mutant protein CRP2(LIM2)R122A causes a conformational rearrangement of the zinc-binding site, which is accompanied by an alteration of packing interactions in the hydrophobic core region and a subsequent change in the relative orientation of the two zinc fingers with a concomitant change in the solvent accessibilities of hydrophobic residues located at the interface of the two modules (24). The structural and possible functional relevance of this residue is indicated by the fact that Arg122 is conserved in all family members of the CRP protein family.

Cross-correlated NMR spin relaxation can be used for structure determination of biomolecules by providing unique “projection constraints” without the need of an empirical calibration (Karplus relation). Examples of protein applications include quantification of dipole–dipole (26–31) and

<sup>†</sup> This research was supported by Grants P13486 (to R.K.) and SFB-F002/211 (to K.B.) from the Austrian Science Foundation (FWF).

<sup>‡</sup> The atomic coordinates and structure factors (code 1IB1) have been deposited in the Brookhaven Protein Data Bank, Brookhaven National Laboratory, Upton, NY.

<sup>\*</sup> To whom correspondence should be addressed at the Institute of Organic Chemistry, University of Innsbruck, Innrain 52a, A-6020 Innsbruck, Austria. Phone: +43-512-507-5240. Fax: +43-512-507-2892. E-mail: robert.konrat@uibk.ac.at.

<sup>§</sup> Institute of Organic Chemistry.

<sup>||</sup> Institute of Biochemistry.

<sup>1</sup> Abbreviations: CRP, cysteine- and glycine-rich protein; LIM, specific double zinc-finger domain; LIM2, carboxyl-terminal LIM domain of CRP protein; *CSRP*, gene encoding CRP protein.

CSA–CSA (32) relaxation interference through recording of double- and zero-quantum coherences. Here we report the application of recently developed CSA–dipole triple-resonance cross-correlated relaxation experiments (29–31) for the refinement of the solution structure of CRP2(LIM2) (together with an increased number of NOE constraints obtained from a  $^{13}\text{C}$ ,  $^{15}\text{N}$  doubly labeled protein sample).

Conformational flexibility is an essential prerequisite for protein function (33–37). For native proteins, internal motions can be either structural fluctuations around local conformational minima or transitions between nearly isoenergetic microstates or conformational substates (36–40). While bond librations occur on fast (picosecond to nanosecond) time scales, correlated displacement of extended segments of the polypeptide chain (41) appears at longer time scales. Over the last years, NMR methodology has been developed to study backbone motions in the microsecond to millisecond time scales (42–47), and the correlation between protein function and structural fluctuations has been experimentally demonstrated (48, 49). Most recently, these studies have been extended to protein side chains (50). Here we use differential  $^{15}\text{N}$ – $^1\text{H}$  and  $^{13}\text{C}$ – $^{15}\text{N}$  multiple-quantum relaxation (51, 52) to identify residues in the wild-type protein CRP2(LIM2) which experience cross-correlated conformational exchange processes. Significant cross-correlated time modulation of backbone isotropic chemical shifts was observed for residues which are connected via an extended hydrogen-bonding network, indicating that CRP2(LIM2) undergoes long-range concerted motions. The existence of multiple conformational substates in a LIM domain indicates that allosteric effects in the course of specific LIM domain–protein interactions may be triggered by a shift in the population of these microstates. The data provide a unique correlation between protein dynamic fluctuations and structural reorientations upon modification of structurally relevant hydrogen-bonding interactions.

## EXPERIMENTAL PROCEDURES

**Protein Preparation and NMR Spectroscopy.** Uniformly  $^{13}\text{C}$ ,  $^{15}\text{N}$ -labeled quail (CRP2)LIM2 was obtained by overexpression in *Escherichia coli* strain BL21(DE3)pLysS as described previously (20, 24), except that 2 g of  $^{13}\text{C}$ -labeled D-glucose (CIL, Andover, MA) was used per liter of culture medium. All NMR experiments were performed on a Varian UNITYPlus 500 MHz spectrometer equipped with a pulse field gradient unit and a triple-resonance probe with actively shielded  $z$  gradients. All spectra were recorded at 26 °C. NMR spectra were processed and analyzed using NMRPipe (53) and ANSIG (54, 55) software. The following spectra were used in the present study for spin system identification and sequential assignment: 2D  $^{15}\text{N}$  HSQC (56), 3D HNCA (57), 3D HNCACB (58), 3D HNCO (59), 3D CBCA(CO)-NH (60), 3D HCCH-TOCSY (61), 3D CCH-TOCSY-NH (62), and two  $^{13}\text{C}$  NOESY-HSQC (63) spectra (centered on  $\text{C}^\alpha$  or methyl). The HCCH-TOCSY was acquired using DIPSI-2 (64) for carbon isotropic mixing. All triple-resonance spectra were performed by including a water flip-back pulse to minimize the effects of radiation damping and solvent (65, 66). Typical carrier positions employed in the double- and triple-resonance experiments were 116 ppm for  $^{15}\text{N}$ , 178 ppm for  $^{13}\text{CO}$ , 58 ppm for  $^{13}\text{C}^\alpha$ , 43 ppm for  $^{13}\text{C}^\beta$ , and 4.68 ppm for  $^1\text{H}$ . Quadrature detection in all of

the indirectly detected dimensions was achieved via States–TPPI (67). For 3D spectra, the number of points was doubled by linear predictions in the indirect dimensions. Cross-correlated relaxation rates involving the  $\text{C}^\alpha$ – $\text{H}^\alpha$  dipolar interaction and the carbonyl ( $\text{C}'$ ) chemical shift anisotropy ( $\Gamma_{\text{C}\alpha(i)\text{H}\alpha(i),\text{C}'(i)}$ ) were measured to access the protein backbone angles  $\psi$  according to the procedure described previously (30). Projection constraints related to the backbone dihedral angles  $\varphi$ ,  $\psi$  were obtained from  $^{15}\text{N}(i)$ – $^1\text{H}^\text{N}(i)$  dipole  $^{13}\text{CO}(i)$  CSA relaxation interference (68). Experimental  $^1\text{H}(i)$ – $^{15}\text{N}(i)$ – $^{13}\text{C}'(i)$  dipole–CSA cross-correlation rates were obtained using the sequence described elsewhere (68). However, only one 3D data set was recorded, leading to an HNCO-type cross-peak, centered at the intrareidue carbonyl frequency and split by the one-bond  $^{15}\text{N}$ – $^1\text{H}^\text{N}$  scalar coupling. Values for  $\varphi$  and  $\psi$  for residues in the metal-coordinating rubredoxin knuckles were extracted from a combination of  $\Gamma_{\text{N}(i)\text{H}(i),\text{C}'(i)}$  and  $\Gamma_{\text{C}\alpha(i)\text{H}\alpha(i),\text{C}'(i)}$  cross-correlation rates by minimizing the difference between experimental and calculated cross-correlation rates independently for each residue. For the calculation of  $\Gamma_{\text{N}(i)\text{H}(i),\text{C}'(i)}$  and  $\Gamma_{\text{C}\alpha(i)\text{H}\alpha(i),\text{C}'(i)}$ , the coordinates of the  $^{15}\text{N}$  solution structure of CRP2(LIM2) (20), standard bond lengths and angles, planar peptide bond geometry, and uniform values for both the components of the  $^{13}\text{C}'$  CSA tensor and the orientation of the tensor with respect to the molecular peptide frame were assumed (69). Differences were determined within the  $(\varphi, \psi)$  interval  $(-180^\circ, 180^\circ)$ . From the set of minima, the nearest minimum to the  $(\varphi, \psi)$  values of the  $^{15}\text{N}$  solution structure (20) was taken. In cases of residual ambiguity,  $^3J_{\text{HNH}\alpha}$  values were used to define the best solution (70). Side-chain dihedral angles  $\chi_1$  were derived from 2D quantitative  $J$ -spectroscopy experiments giving access to  $^3J_{\text{COC}\gamma}$  and  $^3J_{\text{NC}\gamma}$  (71). Cross-correlated conformational exchange processes were identified by recording differential relaxation  $\Gamma_{ij}$  of multiple-quantum coherences as described recently ( $\Gamma_{ij} = R_{\text{DQ}} - R_{\text{ZQ}}$ ) (52, 71), where  $i, j$  denote  $^{15}\text{N}, ^1\text{H}^\text{N}$  or  $^{13}\text{C}', ^{15}\text{N}$ , respectively. Large deviations of the individual DQ/ZQ relaxation differences  $\Gamma_{ij}$  from the average  $\Gamma_{ij}$  values can be taken as measures for the contribution due to cross-correlated time modulation of isotropic chemical shifts (52).

**Structure Calculation.** Three-dimensional structures were generated using experimentally derived NOE constraints from 2D NOESY and 3D  $^{15}\text{N}$  (20) and  $^{13}\text{C}$  NOESY-HSQC in a standard simulated annealing and energy minimization protocol with the CNS (73) software on SGI and Linux workstations. NOE constraints were classified as strong (1.8–2.7 Å), medium (1.8–3.3 Å), weak (2.2–5.0 Å) and very weak (2.2–6.0 Å).

Backbone dihedral angle information was introduced as 27 dihedral angle constraints derived from  $^3J_{\text{HNH}\alpha}$  for  $\varphi$  and Karplus-like potentials applied to the cross-correlation rates for  $\psi$  of the form  $\Gamma_{\text{C}\alpha(i)\text{H}\alpha(i),\text{C}'(i)}(\psi) (\text{s}^{-1}) = A \cos^2(\psi + D) + B \cos(\psi + D) + C$  with the coefficients  $A = 25.5$ ,  $B = -4.27$ ,  $C = -19.1$ , and  $D = -120$  (32 constraints). The Karplus coefficients were obtained on the basis of an overall tumbling time  $\tau_c$  of 6.2 ns. Force constants for  $\Gamma_{\text{C}\alpha(i)\text{H}\alpha(i),\text{C}'(i)}$  cross-correlation structural refinement were employed as described elsewhere (74). The obtained  $(\varphi, \psi)$  angles (obtained from  $\Gamma_{\text{N}(i)\text{H}(i),\text{C}'(i)}$  cross-correlation rates) for residues in the metal-coordinating sites were incorporated in the minimization protocol by employing a force constant of 1.0

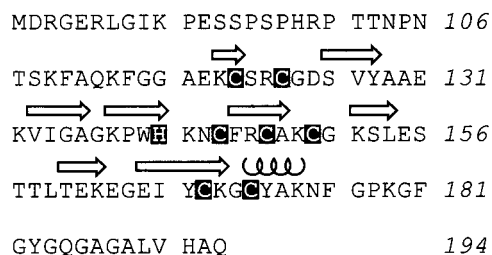


FIGURE 1: Amino acid sequence and alignment of secondary structure elements of CRP2(LIM2). The topology was deduced from the  $^{15}\text{N}$  solution structure of CRP2(LIM2) (20). The zinc-coordinating residues of the CCHC and CCCC zinc-binding sites are shown in reversed type.

$\text{kcal mol}^{-1} \text{ rad}^{-2}$  with a range of  $\pm 20^\circ$  around the restrained angle. Rotational diffusion anisotropy was not incorporated in the derivation of the Karplus coefficients.  $\omega$  dihedral angles were constrained to trans. Side-chain orientation was constrained for nine residues by  $\chi_1$  constraints derived from  $^3J_{\text{NC}\gamma}$  and  $^3J_{\text{COC}\gamma}$  experiments, respectively.

The unstructured N- and C-terminal parts were not considered in the simulations, which were restricted to the central part, residues 117–175, containing the two zinc knuckles. In an initial stage of the structure calculation 642 inter- and intra-NOE restraints were applied to a linearized template structure with extended side chains, where zinc was covalently attached to one of its ligands. Tetrahedral coordination of zinc in the two zinc knuckles C120–C123–H141–C144 and C147–C150–C168–C171 was introduced by NOE constraints connecting the zinc ions to its ligands. Then the zinc ions were covalently attached to the coordinating residues using standard force field parameters (75), and a set of 100 structures was generated. The structures were finally minimized in X-PLOR (76) until convergence by use of the CHARMM force field (77). Structure analysis and calculation of rms deviation values was made with MOLMOL (78).

## RESULTS AND DISCUSSION

**NMR Signal Assignment and Structure Analysis.** The sensitivity-enhanced PFG two-dimensional  $^{15}\text{N}$  HSQC spectrum of  $^{13}\text{C}$ ,  $^{15}\text{N}$ -labeled CRP2(LIM2) was identical to  $^{15}\text{N}$ -labeled CRP2(LIM2) (20) and again demonstrates that CRP2(LIM2) adopts a well-defined structure in aqueous solution. As was found for  $^{15}\text{N}$ -labeled CRP2(LIM2), only secondary backbone amides within the structured region comprising residues Lys119–Gly177 are detectable in the spectra. Again, for residues located in the flexible parts of the polypeptide (residues 82–118 and 178–194) as well as the elongated loop connecting  $\beta$ -strands VI and VII (Glu155–Thr158) (20), no NH connectivities were observed in the  $^{15}\text{N}$ – $^1\text{H}$  HSQC spectra. The availability of additional  $^{13}\text{C}$ -labeling allowed for almost complete assignment of both backbone and side-chain nuclei within the well-structured region of CRP2(LIM2). Secondary structure elements (Figure 1) were confirmed on the basis of characteristic cross-peak patterns in three-dimensional  $^{15}\text{N}$ ,  $^{13}\text{C}$  NOESY-HSQC and two-dimensional NOESY spectra and corroborated by secondary  $^{13}\text{C}^\alpha$  and  $^{13}\text{C}^\beta$  shifts, respectively.

In addition to previously identified strong sequential, intermediate, and long-range NOE connectivities (20), extensive side-chain NOE data not only confirmed the

previously determined CRP2(LIM2) fold but also provided additional important structural constraints. In the  $^{13}\text{C}$ ,  $^{15}\text{N}$  doubly labeled sample 642 distance constraints were applied compared to 393 in the  $^{15}\text{N}$ -labeled sample (20). The NOEs are distributed throughout the entire structure, which suggests an improved coverage of the essential structural features of the CRP2(LIM2) fold by the extended NOE data set.

As it is now well established that cross-correlated spin relaxation experiments can provide structural information about proteins in solution (26–32, 74), cross-correlation rates  $\Gamma_{\text{Ca}(i)\text{Ha}(i),\text{C}'(i)}$  resulting from  $^{13}\text{C}^\alpha$ – $^1\text{H}^\alpha$  dipolar/carbonyl chemical shift anisotropy relaxation mechanisms were used for the refinement of the backbone dihedral angle  $\psi$  (30). Representative examples are shown in Figure 2. A correlation of experimentally obtained cross-correlation rates  $\Gamma_{\text{Ca}(i)\text{Ha}(i),\text{C}'(i)}$  and calculated rates based on the final ensemble of NMR structures are shown in Figure 3. Overall, there is a reasonable agreement between experiment and theory. Only residues in flexible loop or turn regions show some deviations, due to local backbone fluctuations. Residue E163 is located in a flexible turn region connecting the final  $\beta$ -strands ( $\beta$ VII and  $\beta$ VIII; cf. Figure 1) in CRP2(LIM2). The combined use of cross-correlation rates also leads to a significant improvement of the geometry of the metal-binding sites, especially at the terminating residues. The optimized backbone dihedral angles for the residues in the zinc-binding sites of qCRP2(LIM2) are now in better agreement with corresponding residues of other zinc-finger proteins (79–82). In general, only small angle changes were necessary to account for the experimental  $\Gamma_{\text{N}(i)\text{H}(i),\text{C}'(i)}$  and  $\Gamma_{\text{Ca}(i)\text{Ha}(i),\text{C}'(i)}$  dipole–CSA cross-correlation rates. A striking example is the substantial change of backbone dihedral angles for Y172, which was only loosely defined in the  $^{15}\text{N}$ -labeled sample due to a lack of characteristic long-range NOE connectivities.

**Statistical Analysis and Description of Tertiary Structure.** The structural analysis of  $^{13}\text{C}$ ,  $^{15}\text{N}$ -labeled CRP2(LIM2) confirmed the global fold of the previously determined LIM domain on the basis of the analysis of a  $^{15}\text{N}$ -labeled protein sample (20). Most importantly, the increased number of NMR constraints (e.g., in particular constraints for the backbone dihedral angle  $\psi$ ) leads to an improvement of the quality of the obtained structures. Specifically, in the refined set of structures, 81.7% of the residues (excluding the conformationally flexible loop regions; see Table 1) are in the most favored region of Ramachandran space, compared to 72.5% in the best structure of the  $^{15}\text{N}$  solution structure (20). The CCHC and CCCC zinc-binding sites of CRP2(LIM2) in the resulting bundle of energy-minimized structures overlay to the corresponding fragments of the average  $^{15}\text{N}$  solution structure of CRP2(LIM2) (20) with backbone rms deviations of  $1.15 \pm 0.13 \text{ \AA}$  (residues 117–141) and  $1.20 \pm 0.13 \text{ \AA}$  (residues 146–155 and 160–171), respectively. The heavy atom rms deviations (CCHC,  $1.88 \pm 0.15 \text{ \AA}$ ; CCCC,  $2.34 \pm 0.28 \text{ \AA}$ ) indicate a substantial improvement for the C-terminal CCCC subdomain fold, largely due to a change in the orientation of the fold-terminating  $\alpha$ -helix ( $19.8 \pm 16.2^\circ$ ). In Table 1 and Figure 4, the structural statistics, a schematic ribbon drawing, and a superposition of the 15 final structures of quail CRP2(LIM2) are shown. A separate superposition of either the CCHC or the CCCC zinc finger instead of the whole LIM domain results in a decrease of the rms deviation as has already been shown for other CRP



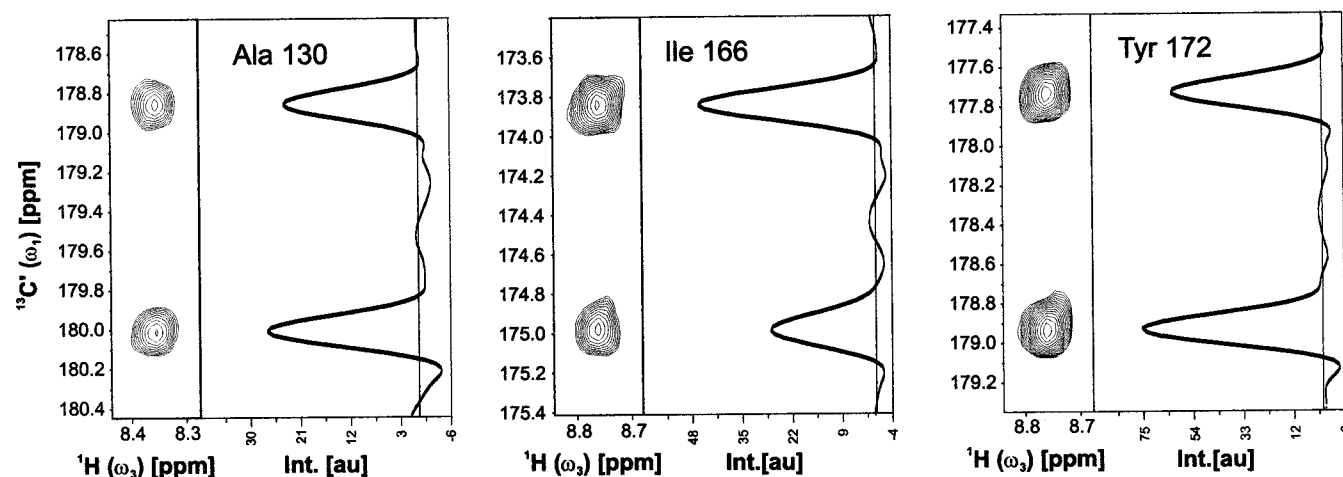


FIGURE 2: Experimental  $\Gamma_{C\alpha(i)Ha(i)C'(i)}$  data for CRP2(LIM2). Cross sections and  $F_1$  slices through Ala130, Ile166, and Tyr172 illustrating experimentally observed differential line broadening for the multiplet components of residues located in  $\beta$ -strand (Ile166),  $\alpha$ -helical (Tyr172), and turn (Ala130) regions in CRP2(LIM2), respectively, are shown.

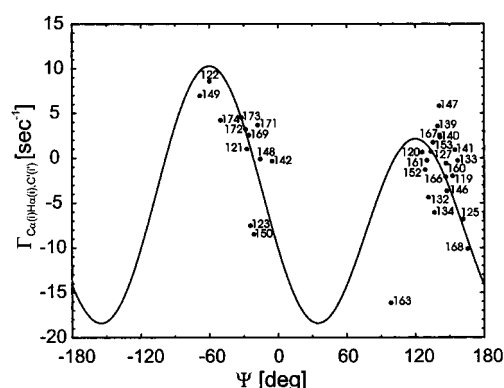


FIGURE 3: Correlation between calculated and experimental values of  $\Gamma_{C\alpha(i)Ha(i)C'(i)}$  for non-glycine residues in CRP2(LIM2). Values of 244, 178, and 90 ppm were used for  $\sigma_{xx}$ ,  $\sigma_{yy}$ , and  $\sigma_{zz}$  (69).

LIM domains (20, 23, 24) and provided evidence for conformational flexibility at the interface of the two zinc-binding modules. The LIM domain fold contains two zinc-finger subdomains terminated by a short  $\alpha$ -helix encompassing residues Cys171–Lys174. The two zinc fingers contain two antiparallel  $\beta$ -sheets connected via flexible loop or turn regions and a rubredoxin-type turn (18) with characteristic hydrogen-bonding pattern (18–24). The additional structural constraints obtained from the doubly labeled CRP2(LIM2) sample allowed for a substantial refinement of the backbone dihedral angles. Specifically, the availability of  $\psi$  angle constraints significantly improved the quality of the derived structure (Table 1 and Figures 3 and 4). From structural analysis of different LIM domains it is evident that side-chain interactions do play a pivotal role in stabilizing the LIM domain fold (18–24). Both hydrophobic interactions within the core region (18–20) and side-chain hydrogen bonding were shown to contribute to the definition of the structure (22, 24). The two zinc-binding modules are packed together via a hydrophobic core which comprises residues Val133, Trp140, Phe145, Leu154, Leu159, and Ile166 (20). Most importantly, the introduction of the  $^{13}\text{C}$ -label allowed for the extraction of additional, structurally important long-range NOEs for Leu154, which was only loosely defined in the previous structure obtained from a  $^{15}\text{N}$ -labeled sample (20).

Table 1: Structural Statistics of CRP2(LIM2)<sup>a</sup>

(A) Experimental Restraints	
distance restraints (total)	642
intraresidue	294
interresidue sequential	161
( $ i - j  = 1$ )	
interresidue medium range	46
( $1 <  i - j  \leq 4$ )	
interresidue long range	141
( $ i - j  > 4$ )	
torsion angle restraints ( $\omega$ )	28 (57)
hydrogen bond restraints	15
(B) Average rms Deviations from Experimental Restraints	
distance restraints ( $\text{\AA}$ )	$0.014 \pm 0.0021$
dihedral restraints (deg)	$0.30 \pm 0.035$
(C) Average rms Deviations from Idealized Covalent Geometry	
bonds ( $\text{\AA}$ )	$0.01 \pm 0.0001$
angles (deg)	$1.98 \pm 0.125$
impropers (deg)	$2.05 \pm 0.383$
(D) X-PLOR Energies <sup>b</sup>	
average $E_{L-J}$ (kcal/mol <sup>-1</sup> )	$-259.3 \pm 12.07$
(E) PROCHECK Summary (Ramachandran Plot) <sup>c</sup>	
% residues in allowed/additionally	
allowed/ generously allowed/	
disallowed regions	
all residues	72.5/23.2/4.0/0.3
loop regions excluded <sup>d</sup>	81.7/14.8/3.5/0.0
(F) Atomic rms Deviation ( $\text{\AA}$ ) <sup>e</sup> (Backbone, Heavy Atoms)	
residues 117–175	$1.24 \pm 0.27, 1.95 \pm 0.25$
residues 117–141	$0.90 \pm 0.25, 1.59 \pm 0.25$
residues 146–155, 160–171	$0.72 \pm 0.16, 1.74 \pm 0.35$

<sup>a</sup> Structural statistics over an ensemble of 15 simulated annealing NMR structures of CRP2(LIM2), calculated with the incorporation of NOE and dihedral angle and H-bond constraints. The NMR structures were calculated for a truncated CRP2(LIM2) sequence, comprising only the structured central LIM domain, residues 117–175. <sup>b</sup>  $E_{L-J}$  is the Lennard-Jones van der Waals energy calculated with X-PLOR using CHARMM force field parameters. <sup>c</sup> Structural quality was checked with PROCHECK (91). In the Ramachandran plot Pro and Gly residues are excluded. <sup>d</sup> The loop regions residues 129–131, 142–144, and 156–159 are excluded. <sup>e</sup> Residues 117–141 and 146–175 encompass the CCHC and CCCC zinc-finger subdomains, respectively, and residues 117–175 represent the entire LIM2 domain of CRP2(LIM2).

**Structural Comparison with CRP2(LIM2)R122A.** A comparison of the tertiary structures of wild-type CRP2(LIM2) and mutant CRP2(LIM2)R122A, in which the hydrogen bond between the side chain of R122 and the zinc-coordinating

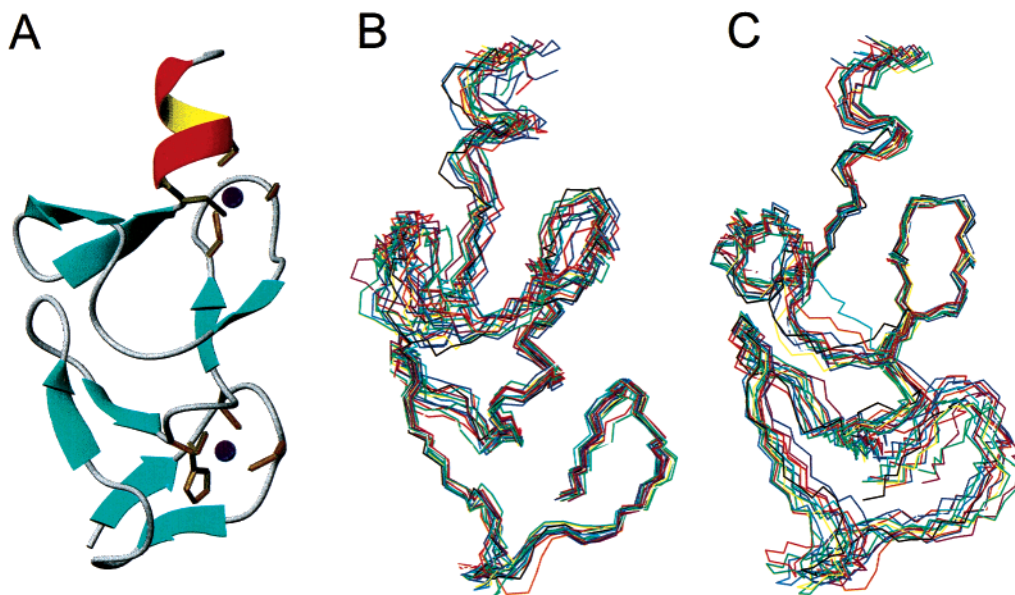


FIGURE 4: Refined solution structure of CRP2(LIM2). Ribbon diagram (A) of a selected representative structure from the calculated set for CRP2(LIM2) (residues 118–174). Separate matches for each of the two zinc-binding sites encompassing residues 120–145 (B) or residues 159–173 (C), respectively, indicate residual mobility between the two zinc-finger subdomains. The diagrams were produced using the program MOLMOL (78).

thiolate of Cys144 was disrupted, showed significant structural differences not confined to the site of mutation (24). The solution structure of the point mutant CRP2(LIM2)-R122A demonstrated that packing interactions in the hydrophobic core and the relative orientation of the two CCHC and CCCC subdomains in an intact LIM domain are not intrinsic rigid features of the domain but can be modified by, for example, the formation or breakage of hydrogen bonds and/or salt bridges, with possible functional implications (e.g., the modulation of LIM domain–homeodomain association, the assembly of a transcription complex, or, in the case of LIM-only proteins, the reversible association with diverse protein binding partners) (24).

To delineate the structural differences between wild-type CRP2(LIM2) and the mutant CRP2(LIM2)R122A and to identify the necessary low-energy conformational changes for this structural reorientation, we have performed an analysis using the program DynDom (83). This program determines clusters of rotation vectors before determining interdomain screw axes and interdomain bending regions and allows to identify structural motifs involved in controlling interdomain motions. Figure 5 shows the results obtained from an analysis using a representative structure of CRP2(LIM2)R122A and the individual structures of the NMR ensemble of doubly labeled CRP2(LIM2). This analysis also demonstrates that the two zinc fingers in the LIM domain constitute to a large extent rigid substructures and that the relative orientation of the two subdomains defines a significant conformational degree of freedom. Interestingly,  $^{15}\text{N}$  relaxation data also indicate a conformational flexibility for the linker region connecting the two rigid substructures (Asn143–Arg146) (20, 24).

**Cross-Correlated Conformational Exchange in CRP2(LIM2).** Cross-correlated conformational exchange processes were identified by recording differential relaxation of  $^{15}\text{N}(i)$ – $^1\text{H}^{\text{N}}(i)$ ,  $\Gamma_{\text{N,H}}$ , and  $^{13}\text{C}'(i-1)$ – $^{15}\text{N}(i)$ ,  $\Gamma_{\text{C',N}}$ , multiple-quantum coherences as described recently (52, 72). The average DQ/ZQ relaxation difference values were as fol-



FIGURE 5: Dynamic domain motion in CRP2(LIM2). The results of the domain decomposition (83) derived from a comparison of the ensemble of NMR solution structures of wild-type CRP2(LIM2) and a representative structure of mutant CRP2(LIM2)R122A (24) illustrate the hinge motion responsible for the change of zinc-finger orientation in CRP2(LIM2). Residues shown in blue, red, and green represent fixed-domain, moving-domain, and bending residues, respectively. Zinc ions are shown as yellow spheres. The orientation of the average interdomain screw axis is shown. The picture was created with the programs DynDom (83) and MOLMOL (78).

lows:  $^{15}\text{N}(i)$ – $^1\text{H}^{\text{N}}(i)$ ,  $2.96 \pm 1.24 \text{ s}^{-1}$ ;  $^{13}\text{C}'(i-1)$ – $^{15}\text{N}(i)$ ,  $-2.5 \pm 1.4 \text{ s}^{-1}$ . In the calculation of the average DQ/ZQ relaxation difference values, the extreme outliers of Figure 6 have been neglected. The observed variations depend on variations of  $^{13}\text{C}'$  and  $^{15}\text{N}$  tensor components (84) and on both fast (picosecond to nanosecond) (72) and slow (microsecond to millisecond) (51, 52) internal motions. Although it is not possible at the moment to unambiguously dissect the structural and dynamical contributions to the differential relaxation of DQ/ZQ, we assume in agreement with theoretic-

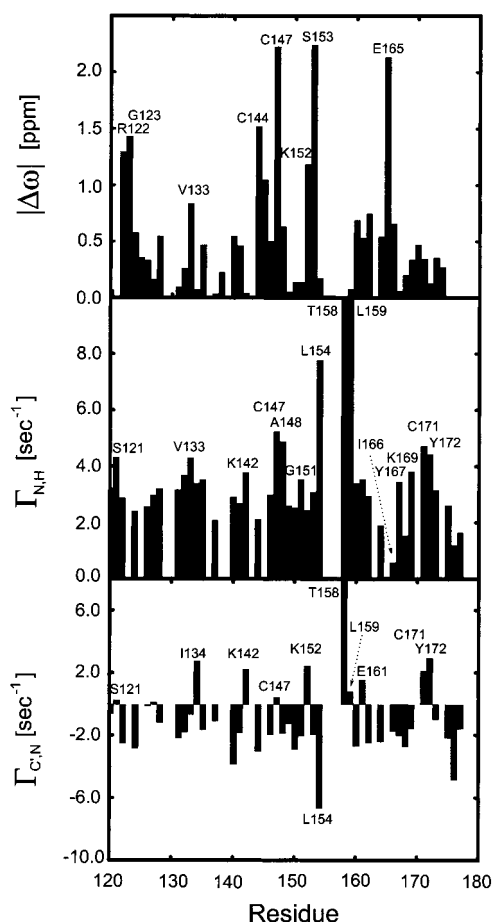


FIGURE 6: Structural changes between CRP2(LIM2) and CRP2-(LIM2)R122A and intramolecular dynamics in CRP2(LIM2). Chemical shift differences between wild-type CRP2(LIM2) and the mutant protein CRP2(LIM2)R122A (24) ( $\Delta\omega = |\Delta\omega(^1\text{H}^N)| + |\Delta\omega(^{15}\text{N})|$ , top) and differential multiple-quantum relaxation ( $\Gamma_{\text{N,H}}$ , middle;  $\Gamma_{\text{C,N}}$ , bottom) are plotted as a function of residue number. Significant deviations from average differential multiple-quantum relaxation ( $\Gamma_{\text{N,H}}$ ,  $2.96 \pm 1.24 \text{ s}^{-1}$ ;  $\Gamma_{\text{C,N}}$ ,  $-2.5 \pm 1.4 \text{ s}^{-1}$ ) indicate contributions from cross-correlated conformational exchange processes.

cal calculations employing a Gaussian distribution of rotational states (72) that the observed variations are predominantly caused by dynamical processes occurring on picosecond to nanosecond time scales. Large deviations from average values, however, are found for residues which undergo conformational exchange processes and display cross-correlated time modulations of the isotropic chemical shifts (51, 52). Note that the fluctuations of the isotropic chemical shifts can be either correlated or anticorrelated, leading to an increase or decrease of the differential line broadening, respectively (52). Figure 6 shows a residue plot of  $\Gamma_{\text{N,H}}$  (middle) and  $\Gamma_{\text{C,N}}$  (bottom) vs residue number. Significant deviations from average  $\Gamma_{ij}$  values were found for the following residues:  $\Gamma_{\text{N,H}}$ , S121, V133, K142, C147, A148, G151, L154, T158, L159, E161, I166, Y167, K169, C171, and Y172;  $\Gamma_{\text{C,N}}$ , S121, S126, V127, I134, K142, C147, K152, L154, T158, L159, E161, C171, and Y172. The experimental finding that significant deviations from average line broadening of both  $^{15}\text{N}(i)-^1\text{H}^N(i)$  and  $^{13}\text{C}'(i-1)-^{15}\text{N}(i)$  multiple-quantum coherences are observed for similar residues indicates the presence of cross-correlated conformational exchange processes at these sites of the polypeptide chain.

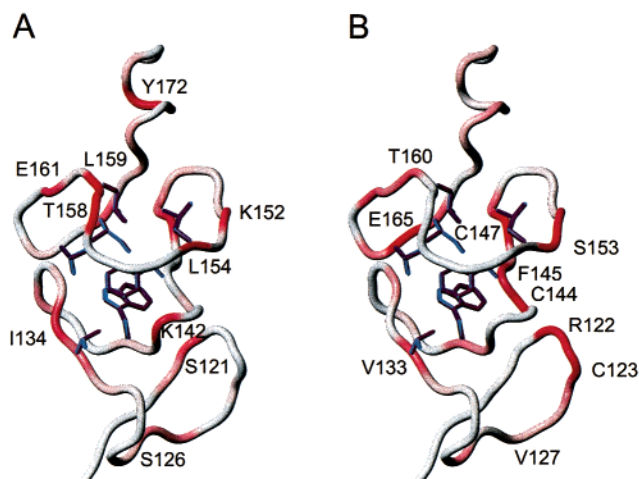


FIGURE 7: Ribbon drawing showing the correlation between cross-correlated millisecond to microsecond time scale motions in CRP2-(LIM2) and structural changes caused by the disruption of the zinc-finger hydrogen bond in CRP2(LIM2)R122A. (A) Residues for which significant cross-correlated millisecond to microsecond time scale motions were observed in wild-type CRP2(LIM2) are displayed on a ribbon representation of a representative structure taken from the ensemble of energy-minimized NMR structures of  $^{13}\text{C}$ ,  $^{15}\text{N}$ -labeled CRP2(LIM2). (B) Location of chemical shift changes introduced by the point mutation R122A. The sum of  $^{15}\text{N}$  and  $^1\text{H}^N$  chemical shift changes [CRP2(LIM2)-CRP2(LIM2)-R122A] were used (24). The side chains of residues located in the hydrophobic core of CRP2(LIM2) (V133, W140, F145, L154, T157, L159, and I166) are shown in blue.

The largest  $\Gamma_{\text{N,H}}$  values were found for T158 and L159. These residues are part of an extended loop connecting two  $\beta$ -strands, and they have been identified as conformationally flexible (20, 52). There is also evidence for conformational flexibility in the two zinc-binding sites. Residues S121, K142 (N-terminal CCHC), C147, A148, G151, K152, and K169 (C-terminal CCCC) show  $\Gamma_{\text{C,N}}$  and  $\Gamma_{\text{N,H}}$  values significantly different from average values. Independent evidence for conformational exchange of residues K142, N143, C144, and C147 was provided by  $^{15}\text{N}$  relaxation (20). Similar observations have been made for the zinc-finger DNA binding domain of Xfin (85) and some of the ligand-binding cysteines of *E. coli* Ada (86). Residues C171 and Y172 are located in the N-terminus of the fold-terminating  $\alpha$ -helix and presumably undergo conformational reorientations reminiscent of helical fraying. Figure 6 (top) also shows chemical shift differences of the backbone signals  $^1\text{H}^N$  and  $^{15}\text{N}$  between wild-type CRP2(LIM2) and mutant CRP2(LIM2)R122A (24). It can be seen that the shift changes (and structural changes) are not confined to the position of the mutation site (R122A) but distributed over the entire protein backbone. It was shown (24) that the disruption of the hydrogen bond between the guanidinium side chain of R122 and the zinc-coordinating thiolate  $\text{S}\gamma(\text{C144})$  leads not only to a conformational rearrangement of the zinc-binding site but also to a change of the packing interactions of the hydrophobic core region and the relative orientation of the two zinc-binding CCHC and CCCC subdomains, respectively. Of particular interest is thus the correlation between the dynamic properties and the structural changes that occur upon disruption of the arginine thiolate side-chain hydrogen bond in CRP2(LIM2)-R122A. Particularly striking is the overlap between the regions of wild-type CRP2(LIM2) exhibiting significant



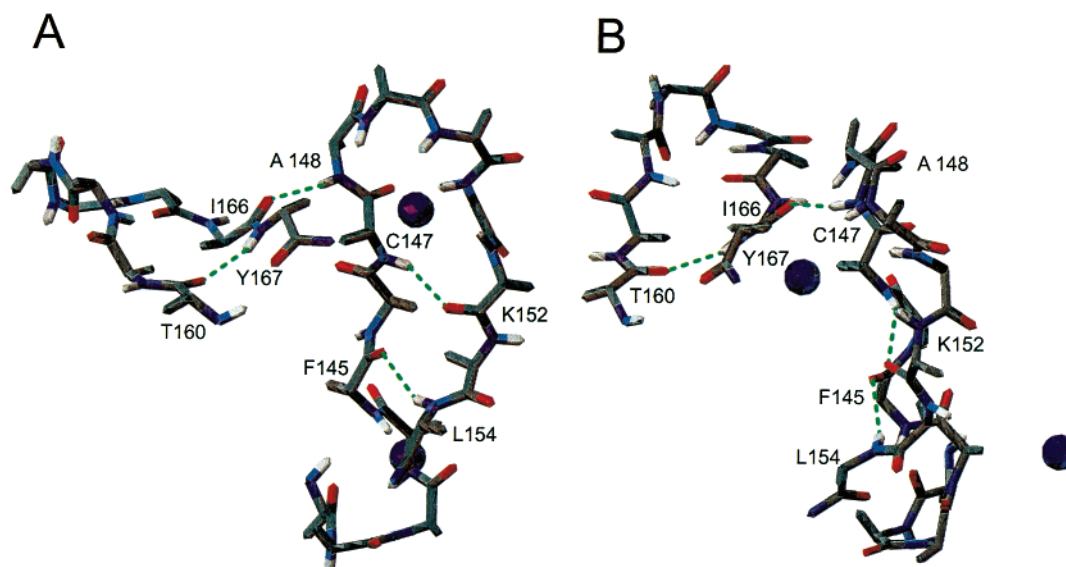


FIGURE 8: Hydrogen-bonding network in CRP2(LIM2). Hydrogen bonds are indicated by dashed lines. Two orthogonal views (A, B) are shown. The hydrogen bond acceptors and donors are labeled according to their residue position. The zinc ions are shown as blue spheres.

conformational exchange (e.g., significantly larger than average  $\Gamma_{ij}$  values) and those which exhibit local structure changes in the mutant protein CRP2(LIM2)R122A (V133, C147, A148, G151, L154, E161, I166, and Y167). Figure 7 shows the location of residues which displayed significantly larger than average DQ/ZQ relaxation differences,  $\Gamma_{C,N}$  and  $\Gamma_{N,H}$  (Figure 7A), and significant chemical shift and local structural changes introduced by the point mutation R122A (Figure 7B). The flexibility of these residues and their structural role in determining the global fold of the LIM domain suggest that they are important in the conformational change that occurs in CRP2(LIM2) upon disruption of the hydrogen bond in the mutant protein CRP2(LIM2)R122A (24). In addition, the conformational plasticity (together with the increased structural resolution provided by the  $^{13}\text{C}$ ,  $^{15}\text{N}$ -labeled sample) also provides an explanation of how the local structural adaptations in the mutant protein are transmitted through the entire protein. In wild-type CRP2(LIM2) there was evidence for interstrand hydrogen bonding between F145–L154, C147–K152, T160–Y167, and A148–I166. Figure 8 shows that these residues are part of an extended hydrogen-bonding network. It thus seems plausible that in wild-type CRP2(LIM2) these residues undergo a long-range concerted motion (on the millisecond to microsecond time scale) involving large  $\beta$ -strand segments of the polypeptide chain. The packing of the side chains (V133, W140, F145, L154, T157, L159, and I166) in the hydrophobic core is also illustrated in Figure 7. The tight packing of the hydrophobic core is also reflected in  $^{13}\text{C}$   $T_1$  and  $T_2$  relaxation times of the methyl groups. For residues which are buried in the hydrophobic core, rather large  $T_1/T_2$  ratios were observed (e.g., L154C $\delta_2$ , 11.1; T157C $\gamma$ , 7.4; I166C $\delta$ , 11.2). Leu159 and V133 are located at the edge of the hydrophobic core and thus appear to be more mobile, which is also indicated by smaller  $T_1/T_2$  ratios (L159C $\delta_{1,2}$ , 3.8, 3.4; V133C $\gamma_{1,2}$ , 1.7, 2.2). The significant DQ/ZQ differential relaxation observed for V133 (Figure 6) is thus presumably due to the fact that V133 is linked to W140 via a hydrogen bond between opposite  $\beta$ -strands ( $\beta$ III and  $\beta$ IV; cf. Figure 1). Residues which are conformationally more flexible typically display

significantly smaller  $T_1/T_2$  ratios (e.g., T160C $\gamma$ , 1.8; V127C $\gamma_{1,2}$ , 2.7, 2.5). The change in the packing interactions of the hydrophobic interface in the mutant protein CRP2(LIM2)-R122A was accompanied by significant  $^1\text{H}$  chemical shift changes of side-chain protons of residues in the hydrophobic core (24). For example,  $^1\text{H}\delta(\text{I166})$  shifted from  $-0.8$  ppm in wild-type CRP2(LIM2) to  $-0.2$  ppm in the mutant protein CRP2(LIM2)R122A. The increased  $T_1/T_2$  ratio of the methyl carbons of Leu154 and I166 is thus very likely due to exchange contributions to  $^{13}\text{C}$  transverse relaxation. The underlying conformational reorientation is presumably a dynamic reordering of the entire hydrophobic core (involving the side chains of W140, F145, L154, and I166) and points to a conformational rearrangement mechanism in CRP2(LIM2) involving backbone and side-chain nuclei. The correlated reordering of both the hydrogen-bonding network and the hydrophobic core can thus be regarded as a significant degree of freedom for CRP2(LIM2) and presumably considered as the reaction coordinate along which the structural reorientation of the mutant protein CRP2(LIM2)-R122A takes place.

**Conclusions.** The structural analysis of the mutant protein CRP2(LIM2)R122A revealed that the relative orientation of the two CCHC and CCCC subdomains in an intact LIM domain is not a rigid feature of the domain but can be altered by the formation and/or breakage of hydrogen bonds (24). The finding that the conformational change between wild-type CRP2(LIM2) and the mutant protein CRP2(LIM2)-R122A is brought about by a collective motion of residues linked together via an extended hydrogen bond network suggests the existence of conformational substates for LIM domains governed by a funnel-like free energy surface (37, 87, 88).

The functional hallmark of LIM domains is the intermolecular interaction with diverse protein-binding partners (7, 10). Specific interactions between LIM domains and proteins involved in the transcriptional machinery have been demonstrated (89–92). The synergistic or allosteric control of these functionally important binding events (93, 94) implies the existence of conformational plasticity in LIM domain



mediated protein recognition reminiscent of Koshland's classical "induced fit" model (95). Alternatively, conformational changes upon ligand or protein binding can be described as a shift in the energy landscape of the folding funnel, leading to a shift in the populations of the substates (96, 97). The present study demonstrates that the predominantly populated conformational substates of an intact LIM domain represent an ensemble of states with different zinc-finger orientations and surface exposure of residues located in the hydrophobic core region, which might be of relevance (19) for the allosteric or synergistic regulation of LIM domain association along physiologically important protein-binding cascades.

## REFERENCES

- Freyd, G., Kim, S. K., and Horvitz, H. R. (1990) *Nature* 344, 876–879.
- Karlsson, O., Thor, S., Norberg, T., Ohlsson, H., and Edlund, T. (1990) *Nature* 344, 879–882.
- Michelsen, J. W., Schmeichel, K. L., Beckerle, M. C., and Winge, D. R. (1993) *Proc. Natl. Acad. Sci. U.S.A.* 90, 4404–4408.
- Michelsen, J. W., Sevell, A. K., Louis, H. A., Olsen, J. I., Davis, D. R., Winge, D. R., and Beckerle, M. C. (1994) *J. Biol. Chem.* 269, 11108–11113.
- Kosa, J. L., Michelsen, J. W., Louis, H. A., Olsen, J. I., Davis, D. R., Beckerle, M. C., and Winge, D. R. (1994) *Biochemistry* 33, 468–477.
- Sánchez-García, I., and Rabbits, T. H. (1994) *Trends Genet.* 10, 315–320.
- Dawid, I. B., Toyama, R., and Taira, M. (1995) *C. R. Acad. Sci. Paris* 318, 295–306.
- Dawid, I. B., Breen, J. J., and Toyama, R. (1998) *Trends Genet.* 14, 156–162.
- Taira, M., Evrard, J.-J., Steinmetz, A., and Dawid, I. B. (1995) *Trends Genet.* 11, 431–432.
- Bach, I. (2000) *Mech. Dev.* 91, 5–17.
- Weiskirchen, R., Pino, J. D., Macalima, T., Bister, K., and Beckerle, M. C. (1995) *J. Biol. Chem.* 270, 28946–28954.
- Arber, S., Halder, G., and Caroni, P. (1994) *Cell* 79, 221–231.
- Arber, S., Hunter, J. J., Ross, J., Jr., Hongo, M., Sansig, G., Borg, J., Perriard, J. C., Chien, K. R., and Caroni, P. (1997) *Cell* 88, 393–403.
- Schmeichel, K. L., and Beckerle, M. C. (1994) *Cell* 79, 211–219.
- Arber, S., and Caroni, P. (1996) *Genes Dev.* 10, 289–300.
- Pomiès, P., Louis, H. A., and Beckerle, M. C. (1997) *J. Cell Biol.* 139, 157–168.
- Harper, B. D., Beckerle, M. C., and Pomiès, P. (2000) *Biochem. J.* 350, 269–274.
- Pérez-Alvarado, G. C., Miles, C., Michelsen, J. W., Louis, H. A., Winge, D. R., Beckerle, M. C., and Summers, M. F. (1994) *Nat. Struct. Biol.* 1, 388–398.
- Pérez-Alvarado, G. C., Kosa, J. L., Louis, H. A., Beckerle, M. C., Winge, D. R., and Summers, M. F. (1996) *J. Mol. Biol.* 257, 153–174.
- Konrat, R., Weiskirchen, R., Kräutler, B., and Bister, K. (1997) *J. Biol. Chem.* 272, 12001–12007.
- Konrat, R., Kräutler, B., Weiskirchen, R., and Bister, K. (1998) *J. Biol. Chem.* 273, 23233–23240.
- Konrat, R., Weiskirchen, R., Bister, K., and Kräutler, B. (1998) *J. Am. Chem. Soc.* 120, 7127–7129.
- Kontaxis, G., Konrat, R., Kräutler, B., Weiskirchen, R., and Bister, K. (1998) *Biochemistry* 37, 7127–7134.
- Kloiber, K., Weiskirchen, R., Kräutler, B., Bister, K., and Konrat, R. (1999) *J. Mol. Biol.* 292, 893–908.
- Yao, X., Pérez-Alvarado, G. C., Louis, H. A., Pomiès, P., Hatt, C., Summers, M. F., and Beckerle, M. C. (1999) *Biochemistry* 38, 5701–5713.
- Reif, B., Hennig, M., and Griesinger, C. (1997) *Science* 276, 1230–1233.
- Pelupey, P., Chiarparin, E., Ghose, R., and Bodenhausen, G. (1999) *J. Biomol. NMR* 14, 277–280.
- Chiarparin, E., Pelupey, P., Ghose, R., and Bodenhausen, G. (1999) *J. Am. Chem. Soc.* 121, 6876–6883.
- Yang, D., Konrat, R., and Kay, L. E. (1997) *J. Am. Chem. Soc.* 119, 11938–11940.
- Yang, D., Gardner, K. H., and Kay, L. E. (1997) *J. Biomol. NMR* 11, 213–220.
- Kloiber, K., and Konrat, R. (2000) *J. Biomol. NMR* 17, 265–268.
- Skrynnikov, N. R., Konrat, R., Muhandiram, D. R., and Kay, L. E. (2000) *J. Am. Chem. Soc.* 122, 7059–7071.
- Karplus, M., and McCammon, J. A. (1981) *CRC Crit. Rev. Biochem.* 9, 293–349.
- Karplus, M., and McCammon, J. A. (1986) *Sci. Am.* 254, 42–51.
- Huber, R., and Bennett, W. S. (1983) *Biopolymers* 22, 261–279.
- Frauenfelder, H., Parak, F., and Young, R. D. (1988) *Annu. Rev. Biophys. Biophys. Chem.* 17, 451–479.
- Frauenfelder, H., Sligar, S., and Wolynes, P. G. (1991) *Science* 254, 1598–1603.
- Ansari, A., Di Iorio, E. E., Dlott, D. D., Frauenfelder, H., Iben, I. E., Langer, P., Roder, H., Sauke, T. B., and Shyamsunder, E. (1986) *Biochemistry* 25, 3139–3146.
- Foot, J., and Milstein, C. (1994) *Proc. Natl. Acad. Sci. U.S.A.* 91, 10370–10374.
- Elber, R., and Karplus, M. (1987) *Science* 235, 318–321.
- Gerstein, M., Lesk, A. M., and Chothia, C. (1994) *Biochemistry* 33, 6739–6749.
- Palmer, A. G. (1997) *Curr. Opin. Struct. Biol.* 7, 732–737.
- Millet, O., Loria, J. P., Kroenke, C. D., Pons, M., and Palmer, A. G. (2000) *J. Am. Chem. Soc.* 122, 2867–2877.
- Loria, J. P., Rance, M., and Palmer, A. G. (1999) *J. Am. Chem. Soc.* 121, 2331–2332.
- Ishima, R., Louis, J. M., and Torchia, D. A. (1999) *J. Am. Chem. Soc.* 121, 11589–11590.
- Akke, M., and Palmer, A. G. (1996) *J. Am. Chem. Soc.* 118, 911–912.
- Mulder, F. A. A., van Tilborg, P. J. A., Kaptein, R., and Boelens, R. (1999) *J. Biomol. NMR* 13, 275–288.
- Kay, L. E. (1998) *Nat. Struct. Biol.* 5, 513–517.
- Feher, V. A., and Cavanagh, J. (1999) *Nat. Struct. Biol.* 400, 289–293.
- Mulder, F. A. A., Skrynnikov, N. R., Hon, B., Dahlquist, F. W., and Kay, L. E. (2001) *J. Am. Chem. Soc.* 123, 967–975.
- Tessari, M., and Vuister, G. W. (2000) *J. Biomol. NMR* 16, 171–174.
- Kloiber, K., and Konrat, R. (2000) *J. Biomol. NMR* 18, 33–42.
- Delaglio, F., Grzesiek, S., Vuister, G., Zhu, G., Pfeifer, J., and Bax, A. (1993) *J. Biomol. NMR* 6, 277–293.
- Kraulis, P. J. (1989) *J. Magn. Reson.* 24, 627–633.
- Kraulis, P. J. (1991) *J. Appl. Crystallogr.* 24, 946–950.
- Kay, L. E., Keifer, P., and Saarinen, T. (1992) *J. Am. Chem. Soc.* 114, 10663–10665.
- Grzesiek, S., and Bax, A. (1992) *J. Magn. Reson.* 96, 432–440.
- Wittekind, M., and Mueller, L. (1993) *J. Magn. Reson., Ser. B* 101, 201–205.
- Kay, L. E., Xu, G.-Y., and Yamazaki, T. (1994) *J. Magn. Reson., Ser. A* 109, 129–133.
- Grzesiek, S., and Bax, A. (1992) *J. Am. Chem. Soc.* 114, 6291–6293.
- Kay, L. E., Xu, G.-Y., Singer, A. U., Muhandiram, D. R., and Forman-Kay, J. D. (1993) *J. Magn. Reson., Ser. B* 101, 333–337.
- Grzesiek, S., Anglister, J., Bax, A., and Bax, A. (1993) *J. Magn. Reson., Ser. B* 101, 114–119.
- Muhandiram, D. R., Farrow, N. A., Xu, G.-Y., Smallcombe, S. H., and Kay, L. E. (1993) *J. Magn. Reson., Ser. B* 102, 317–321.

64. Rucker, S. P., and Shaka, A. J. (1989) *Mol. Phys.* 68, 509–517.
65. Grzesiek, S., and Bax, A. (1993) *J. Am. Chem. Soc.* 115, 12593–12594.
66. Stonehouse, J., Shaw, G. L., Keeler, J., and Laue, E. D. (1994) *J. Magn. Reson., Ser. A* 107, 178–184.
67. Marion, D., Driscoll, P. C., Kay, L. E., Wingfield, P. T., Bax, A., Gronenborn, A. M., and Clore, G. M. (1989) *Biochemistry* 28, 6150–6156.
68. Klotz, K., and Konrat, R. (2000) *J. Am. Chem. Soc.* 122, 12033–12034.
69. Teng, Q., Iqbal, M., and Cross, T. A. (1992) *J. Am. Chem. Soc.* 114, 5312–5321.
70. Vuister, G. W., and Bax, A. (1993) *J. Am. Chem. Soc.* 115, 7772–7777.
71. Vuister, G. W., and Bax, A. (1993) *J. Am. Chem. Soc.* 115, 5334–5335.
72. Pellecchia, M., Pang, Y., Wang, L., Kurochkin, A. V., Kumar, A., and Zuiderweg, E. R. P. (1999) *J. Am. Chem. Soc.* 121, 9165–9170.
73. Brünger, A. T., Adams, P. D., Clore, G. M., DeLano, W. L., Gros, P., Grosse-Kunstleve, R. W., Jiang, J.-S., Kuszewski, J., Nilges, M., Pannu, N. S., Read, R. J., Rice, L. M., Rice, L. M., Simonson, T., and Warren, G. L. (1998) *Acta Crystallogr. D* 54, 905–921.
74. Sprangers, R., Bottomley, M. J., Linge, J. P., Schuktz, J., Nilges, M., and Sattler, M. (2000) *J. Biomol. NMR* 16, 47–58.
75. Lee, M. S., Gippert, G. P., Soman, K. V., Case, D. A., and Wright, P. E. (1989) *Science* 245, 635–637.
76. Brünger, A. T. (1992) *X-PLOR Version 3.1: A System for X-ray Crystallography and NMR*, Yale University Press, New Haven, CT.
77. Brooks, B. R., Brucoleri, R. E., Olafson, B. D., States, D. J., Swaminathan, S., and Karplus, M. (1983) *J. Comput. Chem.* 4, 635–637.
78. Koradi, R., Billeter, M., and Wüthrich, K. (1996) *J. Mol. Graphics* 14, 51–55.
79. Day, M. W., Hsu, B. T., Joshua-Tor, L., Park, J.-B., Zhou, Z. H., Adams, M. W. W., and Rees, D. C. (1992) *Protein Sci.* 1, 1494–1507.
80. Marmorstein, R., Carey, M., Ptashne, M., and Harrison, S. C. (1992) *Nature* 356, 408–414.
81. Fairall, L., Schwabe, J. W. R., Chapman, L., Finch, J. T., and Rhodes, D. (1993) *Nature* 366, 483–487.
82. Omichinski, J. G., Clore, G. M., Schaad, O., Felsenfeld, G., Trainor, C., Appella, E., Stahl, S. J., and Gronenborn, A. M. (1993) *Science* 261, 438–446.
83. Hayward, S., and Berendsen, H. J. C. (1998) *Proteins* 30, 144–154.
84. Sitkoff, D., and Case, D. A. (1998) *Prog. Nucl. Magn. Reson. Spectrosc.* 32, 165–190.
85. Palmer, A. G., III, Rance, M., and Wright, P. E. (1991) *J. Am. Chem. Soc.* 113, 4371–4380.
86. Habazettl, J., Myers, L. C., Yuan, F., Verdine, G. L., and Wagner, G. (1996) *Biochemistry* 35, 9335–9348.
87. Bryngelson, J. D., and Wolynes, P. G. (1989) *J. Phys. Chem.* 93, 6902–6915.
88. Dill, K. A., and Chan, H. S. (1997) *Nat. Struct. Biol.* 4, 10–19.
89. Bach, I., Rhodes, S. J., Pearse, R. V., II, Heinzel, T., Gloss, B., Scully, K. M., Sawchenko, P. E., and Rosenfeld, M. G. (1995) *Proc. Natl. Acad. Sci.* 92, 2720–2724.
90. Jurata, L. W., Kenny, D. A., and Gill, G. N. (1996) *Proc. Natl. Acad. Sci. U.S.A.* 93, 11693–11698.
91. Wadman, I. A., Osada, H., Grütz, G. G., Agulnick, A. D., Westphal, H., Forster, A., and Rabbits, T. H. (1997) *EMBO J.* 16, 3145–3157.
92. Johnson, J. D., Zhang, W., Rudnick, A., Rutter, W. J., and German, M. S. (1997) *Mol. Cell. Biol.* 17, 3488–3496.
93. Xue, D., Tu, Y., and Chalfie, M. (1993) *Science* 261, 1324–1328.
94. Lichtsteiner, S., and Tijan, R. (1995) *EMBO J.* 14, 3937–3945.
95. Koshland, D. E., Jr. (1958) *Proc. Natl. Acad. Sci. U.S.A.* 44, 98–123.
96. Tsai, C. J., Kumar, S., Ma, B., and Nussinov, R. (1999) *Protein Sci.* 8, 1181–1190.
97. Tsai, C. J., Ma, B., and Nussinov, R. (1999) *Proc. Natl. Acad. Sci. U.S.A.* 96, 9970–9972.
98. Laskowski, R. A., MacArthur, M. W., Moss, D. S., and Thornton, J. M. (1993) *J. Appl. Crystallogr.* 26, 283–291.

BI010509M